



DIAGNOSTICS OF CORONAL HEATING IN ACTIVE-REGION LOOPS

A. FLUDRA¹, C. HORNSEY^{1,2}, AND V. M. NAKARIAKOV²

¹ RAL Space, STFC Rutherford Appleton Laboratory, Harwell, Didcot, OX11 0QX, UK

² Physics Department, University of Warwick, Coventry, CV4 7AL, UK

Received 2016 March 2; revised 2016 November 4; accepted 2016 November 8; published 2017 January 5

ABSTRACT

Understanding coronal heating remains a central problem in solar physics. Many mechanisms have been proposed to explain how energy is transferred to and deposited in the corona. We summarize past observational studies that attempted to identify the heating mechanism and point out the difficulties in reproducing the observations of the solar corona from the heating models. The aim of this paper is to study whether the observed extreme ultraviolet (EUV) emission in individual coronal loops in solar active regions can provide constraints on the volumetric heating function, and to develop a diagnostic for the heating function for a subset of loops that are found close to static thermal equilibrium. We reconstruct the coronal magnetic field from *Solar Dynamics Observatory*/HMI data using a nonlinear force-free magnetic field model. We model selected loops using a one-dimensional stationary model, with a heating rate dependent locally on the magnetic field strength along the loop, and we calculate the emission from these loops in various EUV wavelengths for different heating rates. We present a method to measure a power index β defining the dependence of the volumetric heating rate E_H on the magnetic field, $E_H \propto B^\beta$, and controlling also the shape of the heating function: concentrated near the loop top, uniform and concentrated near the footpoints. The diagnostic is based on the dependence of the electron density on the index β . This method is free from the assumptions of the loop filling factor but requires spectroscopic measurements of the density-sensitive lines. The range of applicability for loops of different length and heating distributions is discussed, and the steps to solving the coronal heating problem are outlined.

Key words: Hydrodynamics – magnetic fields – Sun: atmosphere – Sun: corona – Sun: UV radiation

1. INTRODUCTION

The question of what heats the plasma in the magnetically - closed solar corona to kinetic temperatures over one million kelvin is one of the most important unsolved problems in astrophysics. The basic building blocks of the corona are ubiquitous magnetic loops filled with hot, fully ionized plasma. The solution to the coronal heating problem lies, therefore, in understanding the heating of coronal loops. The energy source for heating is the kinetic energy of plasma flows driven by thermal convection in the photosphere. The mechanical motions in and below the photosphere displace the footpoints of coronal field lines and can generate magnetic stresses or waves, leading to two broad classes of heating models, direct current (DC) and alternate current (AC) models (Aschwanden 2004; Klimchuk 2006). In most models, the magnetic field strength B is the primary quantity determining the heating rate.

The theory of coronal heating has been studied extensively (see reviews by Narain & Ulmschneider 1996; Walsh & Ireland 2003; Klimchuk 2006). Observational tests, however, have been difficult to obtain, and there is a great need to provide stringent observational constraints on the heating models.

The continuing progress in the development of solar X-ray and EUV instrumentation and the availability of a large number of extreme ultraviolet (EUV) and X-ray observations of active regions from solar missions such as Skylab, Yohkoh, *SOHO*, and TRACE enabled the first tests of the coronal heating theories. Spectral line intensities depend directly, albeit nonlinearly, on the energy input (heating rate), so finding how they depend on the magnetic field is key to testing the heating models. Pioneering work by, for example, Gurman et al. (1974), Golub et al. (1980), Fisher et al. (1998), and Pevtsov et al. (2003) used spatially integrated intensities in EUV lines

or X-ray bands and compared them with the photospheric magnetic flux measurements.

Fludra & Ireland (2003, 2008) extended the study of these global relationships in a large number of active regions observed by the *SOHO* Coronal Diagnostic Spectrometer. From this statistical analysis, Fludra & Ireland (2008) obtained clear power laws between the active-region integrated magnetic flux and EUV emission line intensities, and they critically analyzed their capability to constrain the heating rate. They demonstrated that the global power-law analysis is only an approximation of the true relationship between the observed line intensities and the magnetic fields, not based on a mathematically rigorous approach. A correct analysis procedure is derived in Fludra & Ireland (2003). The global analysis gives the dependence of the volumetric heating rate, E_H , on the photospheric magnetic flux density, ϕ : $E_H \propto \phi^\gamma$, where $0.6 \leq \gamma \leq 1.1$, assuming loops are in static equilibrium.

A subsequent study by Fludra & Warren (2010) for the first time compared fully resolved images in an EUV spectral line of O V 63.0 nm with the photospheric magnetic field, leading to the identification of a dominant, ubiquitous variable component of the transition region EUV emission ($T_e \approx 2 \times 10^5$ K) and a discovery of a steady basal heating, and they derived the following dependence of the basal heating rate on the photospheric magnetic flux density and loop length L : $E_H \propto \phi^{0.5} L^{-1}$.

In the above studies, the emphasis was on statistical correlations between radiative and magnetic quantities in a large number of active regions. Since the publication of the coronal loop models by Rosner, Tucker & Viana (1978), another series of papers carried out simulations of the coronal magnetic fields and modeling of the expected X-ray or EUV emission for different coronal heating models in large loop

ensembles. These studies continued using the simplest assumptions of thermally stable loops, uniform heating, and constant loop cross section. A substantial study was done by Schrijver & Aschwanden (2002), who derived potential magnetic field extrapolations of the entire Sun and Sun-like stars. The heating rate was proportional to the magnetic flux density at loop footpoints to a power of β and depended on other loop parameters. The statistical constraints on the models were provided by the distributions of temperature and X-ray emission levels observed in the solar and stellar coronae and the relationships between disk-averaged radiative and magnetic flux densities. This study, wide and ambitious in its scope, showed that the heating models can be constrained to some degree, and further progress can possibly be made by restricting the analysis to smaller areas, such as solar active regions.

Warren & Winebarger (2006) analyzed 26 active regions observed by Yohkoh/SXT and *SOHO*/EIT. Using potential magnetic field extrapolations and hydrostatic models, they simulated intensity along the loops using a uniform heating rate dependent on the magnetic field strength B_a averaged along the field line, to the power of $\alpha = 0, 1$, or 2 . The parameters of this study gave the loop peak temperature of 4 MK. Comparing simulated X-ray SXT images with observations, they obtained $\alpha = 1$ and concluded that the hot SXT loops are consistent with static models. For EIT, α was difficult to determine in the range 0–2, and the simulated images did not agree with observations and contained mostly moss (i.e., emission arising from the lowest segments of loops) because the loop-top temperatures were significantly above the temperatures of peak emissivities of the EUV bands and did not reproduce the observed EIT images well.

Subsequently, Warren & Winebarger (2007) analyzed one active region, using two cases: first, the potential magnetic field and a hydrostatic model with a constant cross section and uniform heating, the same as in Warren & Winebarger (2006); and second, using a hydrodynamic model with time-variable heating. In both cases, the X-ray emission observed by the Yohkoh/SXT was reproduced well. There was some improvement in reproducing the EUV bands of EIT when using the dynamic model, but the agreement with observations was still not acceptable.

Lundquist et al. (2008a) modeled one active region using nonlinear force-free magnetic field extrapolations. The energy equation used steady-state heating, steady flow, and an expanding loop cross section. The heating rate was still uniform though, dependent on the magnetic field B_a averaged along the loop, and they considered four cases, with the heating proportional to B_a/L , B_a/L^2 , B_a^2/L , B_a^2/L^2 . A comparison of the synthetic images with Yohkoh/SXT X-ray observations demonstrated the complexity of such a task, with many factors affecting the overall agreement: matching the reconstructed magnetic field lines to the shapes of observed loops, choosing the required filling factors to match the overall emission levels, obtaining the best visual agreement between the morphology of the modeled and observed emission, and using a different set of model parameters to match the observed filter-ratio temperatures of approximately 4 MK. Subsequently, these authors tested an exponentially decreasing heating rate of $E_H = E_0 \exp(-s/s_H)$, where a negative scale height, s_H , simulated apex heating, and they found that the apex heating gives a better match to temperature and emission measures,

while the image prediction quality was better for a footpoint heating. Generally, the results were sensitive to the parameters defining the heating rate, confirming that this remains a promising avenue for further exploration of the heating mechanisms.

Lundquist et al. (2008b) applied the method from Lundquist et al. (2008a) to 10 active regions. Testing four uniform heating rates, the heating rate proportional to B_a/L (B_a is averaged along the loop) gave the best prediction of temperatures derived from filter ratios. However, they concluded that their forward models are poor in representing observations, and it is possible that the inclusion of the transient heating may be necessary.

An important step in testing the heating models was the transition from the assumptions of uniform heating to nonuniform heating, allowing the investigation of the location of the heating along the loop and a possible dependence of the heating rate on the local magnetic field strength. These studies developed in parallel to the previously discussed papers.

One of the most thorough studies of individual loops was made by Aschwanden et al. (2001), who explored hydrostatic solutions of coronal loops with nonuniform heating and constant cross section, for loops with loop-top temperatures of 1.0–1.3 MK as observed by TRACE in the EUV wavelengths 171 Å and 195 Å. They found that 30% of 41 observed loops are consistent with steady-state solutions. The remaining loops must be evolving, showing significant overpressure (a few show underpressure) compared to hydrostatic solutions. Aschwanden et al. (2001) applied a heating function decaying exponentially from the footpoint toward the apex, with a scale height s_H . They found that shorter heating scale heights give higher densities, and comparing with observations they concluded that the 12 loops observed to be in equilibrium have heating concentrated near the footpoints, with the heating scale height 12 ± 5 Mm and the ratio of the heating scale height to the loop half-length in the range 0.22 ± 0.11 . Figure 2 in Aschwanden et al. (2001) shows that for heating scale heights below a critical value there are no solutions of the hydrostatic equation. This is caused by thermal instability, which will be further discussed in Section 3.3. They conclude that the measurement of the pressure or density in a loop allows a diagnostic of the physical state of the loop (steady-state equilibrium or dynamical evolution).

The solutions of the hydrostatic loop models for the heating concentrated near the footpoints were studied further by Winebarger et al. (2003). Assuming again a constant loop cross section, they found that the footpoint heating can increase the density in a loop by a factor of up to 3 over a uniform heating, while the apex heating decreases the density by a factor of 2.5 compared to uniform heating. They confirmed that no more than 28% of loops observed by TRACE and Yohkoh/SXT can be interpreted as static loops.

Dudik et al. (2011) investigated whether observations in EUV and X-ray filters can be modeled simultaneously under the assumption of steady heating and potential field extrapolations. They used a spatially variable heating rate along the loop, characterized by a heating scale length, calculated hydrostatic models, and compared the modeled emission to observed emission simultaneously in the *SOHO*/EIT 171, 195, and 284 bands and X-ray emission in Hinode/XRT. The best overall agreement is obtained when the models include a variable loop cross-section expansion. They find very short heating scales

and unstable solutions in the 171 and 195 Å filters, and larger heating scales and stable solutions in the 284 and X-ray filters.

A substantial refinement and update of these studies has been made by Mikic et al. (2013), who used a one-dimensional (1D) hydrodynamic model with variable cross section proportional to $1/B(s)$, where $B(s)$ is the magnetic field strength along the loop. Mikic et al. (2013) considered the effect of varying loop parameters on the loop model solutions. In particular, they concluded that a variable cross-section area must be used for the correct derivation of densities (the modeled density at the apex was 76% larger when compared to the constant area case). However, a variable cross section makes the loop more likely to produce thermal nonequilibrium solutions. They also point out that real loops with a nonsymmetric distribution of $B(s)$ and nonsymmetric heating have incomplete, less massive condensations when in thermal nonequilibrium and better agree with observations.

Based on the study by Mikic et al. (2013), Lionello et al. (2013) calculated a three-dimensional (3D) hydrodynamic model of one active region using *SOHO*/MDI magnetograms. They assumed a steady heating function from Rappazzo et al. (2008), $E_H \propto B^{7/4}$, that represents heating through turbulent dissipation of magnetic energy and is strongly localized near the footpoints. Using simulated *SOHO*/EIT and Hinode/XRT images and Fe XIII density-sensitive spectral lines from Hinode/EIS, they found that the distributions of electron densities in two loops are flatter and 4.9 and 3.8 times higher at the apex than in a steady-state solution with a uniform heating and the same peak temperature of 1.6 MK. The characteristics of simulated loops agree qualitatively with observations. They concluded that a steady heating concentrated at footpoints, driving thermal nonequilibrium solutions, may be responsible for the heating of the EUV loops. In view of our results in Section 3, thermal instability is to be expected for the form of the heating function used by Lionello et al. (2013). That paper also demonstrated the importance of using spectroscopically determined densities to identify nonequilibrium solutions.

The papers summarized above suggest that observations of many EUV loops are difficult to reproduce using the standard assumptions of static loop models. There are strong indications that these loops are heated predominantly near the footpoints, which then may trigger thermal instability. However, a full answer to the question how the EUV loops are heated has not been found yet. For completeness, we mention that several parallel studies proceeded to investigate particular dynamic heating scenarios (for example, heating by nanoflares as suggested by Parker 1988). Other more recent studies employ full 3D MHD codes, modeling the dynamic evolution of active-region magnetic fields and the thermodynamic properties of plasma confined by the field lines (e.g., Galsgaard & Nordlund 1996; Gudiksen & Nordlund 2005; Hansteen et al. 2015). These numerical simulations assume energy deposition from resistive dissipation (Joule heating) and manage to reproduce the qualitative structure and evolution of coronal loops over active regions fairly well. One can envisage that, with growing computational power, increasing the 3D volume size and the spatial resolution, these simulations may become a useful tool for a quantitative comparison with observations and diagnostics of individual loops in the future.

Several studies described above concluded that the statistical analysis of whole active regions or full-disk images does not

give sufficient agreement of models with observations. We will address the reasons in Section 3.3. In the present paper we address the unsolved aspects of the coronal heating problem of EUV loops by returning to basics and investigating the diagnostics of individual coronal loops. In a most general approach, one would assume that the heating is variable in time and leads to a dynamic behavior of the plasma confined in coronal loops. Such radiative hydrodynamic loop models with different forms of the heating rate have been studied by many authors (see Reale 2014 for review). However, since the temporal variability of the heating rate needs to be arbitrarily prescribed, it adds an additional degree of freedom, increasing the complexity of the problem. In this paper we are addressing the ability of the coronal EUV observations to provide constraints on models, so we begin with simpler, stationary models, reducing significantly the number of model parameters, as done also in the majority of the studies quoted above. In this way, we are able to study the effect of the spatial variability of the heating rate along the loop on the resulting EUV emission without the complications of the temporal variability. We aim to apply this to those loops that are tractable by this method.

The aim of this paper is to develop a diagnostic of the heating mechanisms in coronal loops and evaluate the capability of the observed coronal EUV emission to provide constraints on the parameters of the heating model. We choose to provide this for a class of loops that meet the stationary conditions. Even though only about 30% of loops observed in the EUV range at wavelengths 171 and 195 Å are consistent with steady-state loop models (Aschwanden et al. 2001; Winebarger et al. 2003), this is a sufficiently large fraction to justify the inquiry into their heating mechanism. Deriving a diagnostic to solve the question of how these loops are heated would be an important step toward understanding the coronal heating. We go beyond previous analyses by using nonlinear force-free (NLFF) magnetic field extrapolations, an expanding loop cross section, linking the heating rate to the local values of the magnetic field strength along real loops, and applying a parametric dependence on B that regulates the concentration of the heating between the footpoints and the top of the loop. This provides a more realistic approximation than using an arbitrary scale height for the decrease of the heating rate along the loop.

We proceed by modeling a coronal active region, first by extrapolating its coronal magnetic field from the photospheric field, then using a 1D hydrostatic model to derive plasma parameters in selected field lines of this active region. This model allows an arbitrary heating rate, which was chosen to be a function of the local magnetic field strength.

The *Solar Dynamics Observatory* (*SDO*) provides a unique opportunity to perform this study using two of its instruments, the magnetograph HMI (Scherrer et al. 2012) and the EUV imager Atmospheric Imaging Assembly (AIA) (Lemen et al. 2012). HMI provides full-disk vector magnetograms with $1'' \times 1''$ pixel size every 12 minutes. This allows accurate measurements of the photospheric magnetic field for any active region, which is a basis for performing NLFF extrapolations (Schou et al. 2012). AIA provides full-disk EUV images in seven different filters every 12 seconds, with a pixel size of $\sim 0.6'' \times 0.6''$.

We calculate force-free magnetic field extrapolations of the HMI magnetograms using the numerical code described in Wiegmann (2004) and derive the values of the magnetic field

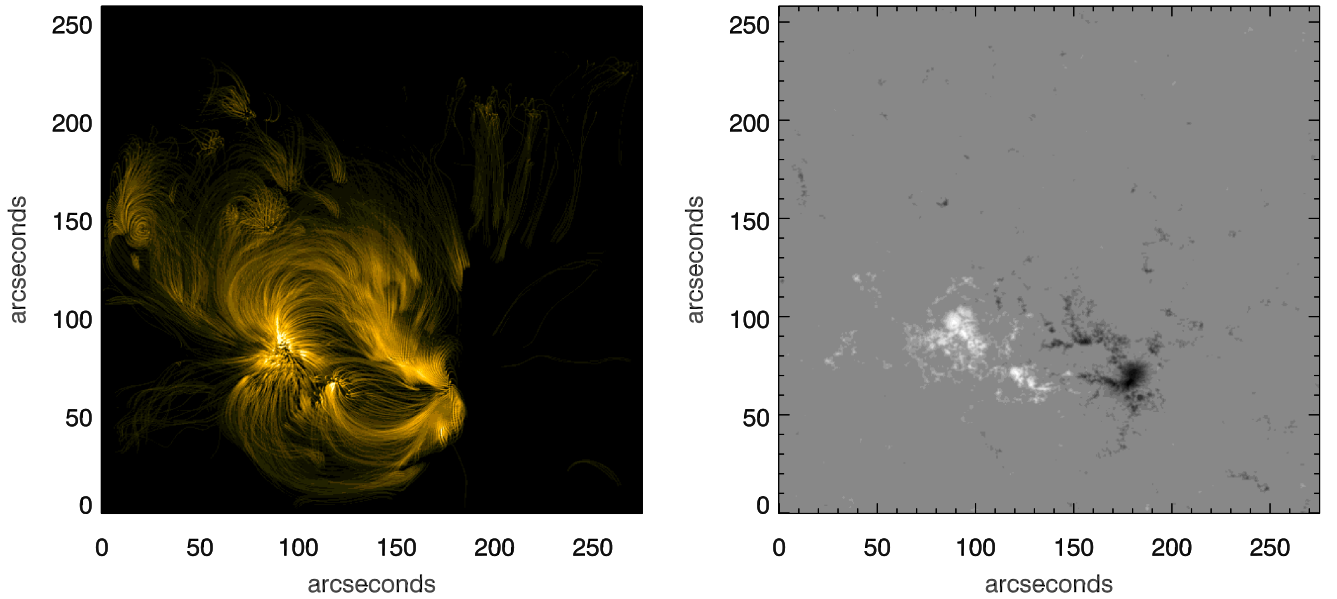


Figure 1. Left: example of an active region NOAA 11897 modeled in *SDO*/AIA 171 Å filter for $\beta = 0.5$. See text for details. Right: *SDO*/HMI magnetogram of the same active region observed on 2013 November 4.

strength B along all coronal loops. We then calculate stationary loop models with subsonic flows for each magnetic field line using a method described in Schrijver & van Ballegooijen (2005), which allows an arbitrary magnetic field strength $B(s)$ and coronal heating rate $E_H(s)$ as functions of position s along the loop. Exploring a range of different forms of the heating function, the modeled coronal loop density, N_e , and electron temperature, T_e , are then used to predict the intensities of the spectral lines of the Fe IX 171 Å, Fe XVI 335 Å, and *SDO*/AIA passbands.

In this paper we address the basic principles of the coronal heating diagnostics, without complicating the study with well-known observational problems, such as instrumental point-spread functions, line-of-sight confusion and background subtraction, scattered and stray light contributions, or possible spectral line blends. Such effects add an additional layer of complexity when the method is eventually applied to real data, but they are the property of the observations due to instrumental effects and the complexity of the multiloop corona, not of the underlying heating processes, and would obscure the fundamental question about the existence and limitations of the method itself we wish to answer. The application of the method to real data and the inclusion of these effects are deferred to a separate paper.

This paper is arranged as follows. In Section 2 we discuss the NLFF extrapolations and the steady-state loop modeling, leading to a simulation of the EUV emission. In Section 3 we apply these models to four loops from an active region, describe the diagnostic method, and test a variety of heating rates. Conclusions are given in Section 4.

2. METHOD

2.1. Magnetic Field Extrapolations

A typical method of extrapolating photospheric magnetic fields into the corona is a nonlinear force-free field model. It makes the assumption that the corona is a force-free

environment (Gary 2001). Force-free fields obey

$$\mathbf{j} \times \mathbf{B} = 0, \quad (1)$$

$$\nabla \times \mathbf{B} = \mu_0 \mathbf{j}, \quad (2)$$

$$\nabla \cdot \mathbf{B} = 0. \quad (3)$$

Various methods have been proposed to find solutions to this nonlinear system of equations (e.g., Sakurai 1981; Roumeliotis 1996; Amari et al. 1997; Wheatland et al. 2000, Aschwanden 2013).

The bottom boundary conditions for the NLFF extrapolation were vector magnetograms obtained from *SDO*/HMI. These contained the vector photospheric magnetic field data with a $1'' \times 1''$ resolution. A typical size of the box surrounding the active region is 5×5 arcmin, leaving a sufficient margin around the active-region magnetic fields to include all of the strong magnetic field lines as they expand into the corona. An NLFF model was then used to extrapolate this field into the corona to give an estimate of the coronal magnetic field.

The NLFF model is calculated using the optimization code developed by Wiegmann (2004) and tested with *SDO* data (Wiegmann et al. 2012). Schrijver et al. (2006) and Metcalf et al. (2008) compared different NLFF magnetic field models and found that the optimization code was the most accurate model tested, as well as being reasonably computationally efficient. While Schrijver et al. (2008) showed that other codes may perform better in other circumstances, we use the extrapolations only to select several plausible magnetic loops, and an exact match to the observed EUV loops is not investigated. Despite performance differences between different NLFF codes, it is generally believed that the NLFF extrapolations provide a more accurate structure of the coronal magnetic field than potential extrapolations.

This procedure provides a model for the coronal magnetic field of the active region. The next stage is to define the loops traced by this field. We trace a field line from each pixel in the base of our field. To do this, we use a fourth-order Runge-Kutta scheme to calculate the direction at each step of the field line by using the direction of the local magnetic field as the line's gradient. As this study is only interested in coronal loops,

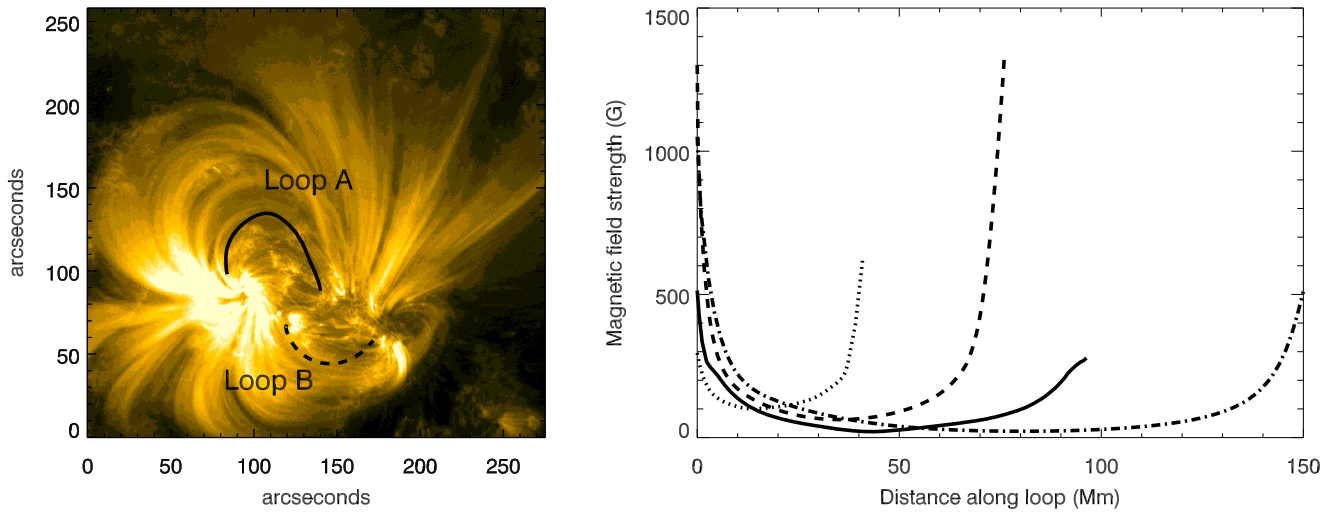


Figure 2. Left: *SDO*/AIA image of active region NOAA 11897 in 171 Å filter, observed on 2013 November 4. Black lines show the NLFF modeled loops that were studied further. The solid line is loop A, and the dashed line is loop B. Right: the magnetic field strength along loop A (solid line), loop B (dashed line), loop C (dot-dashed line), and loop D (dotted line). These line styles are kept consistent throughout this paper.

we discard those loops that do not reach a coronal height (2000 km), as well as those loops that could not be traced from photosphere to photosphere (i.e., those that left the sides or top of the box containing the modeled magnetic field).

Figure 1(a) shows a modeled AIA 171 image for the considered active region, and the HMI magnetogram for this region is shown in Figure 1(b). From the modeled magnetic field, four loops were chosen for further study. For clarity, only two of these loops, denoted A and B, are shown in Figure 2(a). Loop A is in the upper fan of loops in this active region, while loop B is in the downward fan. Loop B is fairly short ($L = 76$ Mm), and its magnetic field appears to be very symmetric about the loop top, as well as fairly strong at its footpoints, with a magnetic field strength of ~ 1300 G. Loop A is slightly longer ($L = 95$ Mm) with a weaker and much less symmetric field, ~ 500 G in one footpoint and ~ 280 G in the other footpoint. Loop C is an example of a longer loop, in a location in the active region similar to loop B, but 150 Mm in length and with a magnetic field strength slightly larger than that of loop A. Loop D is the shortest of the four loops, at roughly 40 Mm long. It is located close to loop B in the active region, and its magnetic field strength distribution differs from the other three loops, as will be discussed in Section 3.1. Loops C and D allow us to consider the effect of varying the loop length. All four loops have magnetic field strengths fairly typical for loops in this active region. A comparison of the field strengths along all four loops considered in detail is shown in Figure 2(b).

2.2. Loop Models

Once the magnetic topology has been defined by the NLFF model, the plasma in the loops is modeled to derive electron temperature, density, and flow velocities.

As stated in Section 1, our goal is to investigate cases of quasi-static loops, where the heating is either constant in time or varies with a timescale shorter than the typical radiative cooling and thermal conduction timescales. Many such models are described in the literature (Rosner et al. 1978; Vesecky et al. 1979; Reale et al. 2000).

We use a loop model code developed by van Ballegooijen (Schrijver & van Ballegooijen 2005). This code finds a stationary solution with subsonic flows to the energy-balance

equation in 1D and allows for an arbitrary heating rate along the loop. It models the loop from the transition region at the first footpoint through the corona and back to the transition region at the second footpoint. The loop parameters, therefore, do not need to be symmetric. It sets the temperature at each footpoint to 20,000 K, twice the temperature of the chromosphere. The energy flux through the boundary is calculated in the appendix of the cited paper. The model also assumes that the loop cross section is inversely proportional to the local magnetic field strength.

For this study, we use a volumetric heating rate of the following form:

$$E_H(s) = Q_a L^\lambda \left(\frac{B(s)}{B_{\max}} \right)^\beta, \quad (4)$$

where $B(s)$ is the magnitude of the magnetic field at distance s along the loop, and B_{\max} is a constant, set to be 2500 G for this study. This gives three parameters to control the heating rate, Q_a , β , and λ . We assume $\lambda = -1.0$ as suggested by Fludra & Warren (2010) from the analysis of the transition-region emission. We point out that Schrijver et al. (2004) obtained the energy flux into the loops $F_H \propto B_{\text{phot}}/L$ erg cm $^{-2}$ s $^{-1}$ from hot coronal emission, which under their assumption of uniform volumetric heating would give $E_H = F_H/L$ and $\lambda = -2$. The value of the parameter λ will not be investigated further because in this study we are only interested in looking at one single loop at a time, and any change in the loop length L or λ can be absorbed by a change in Q_a . The absolute scaling of E_H is therefore controlled by Q_a , and we vary only two parameters, Q_a and β . However, varying the loop length does have an effect on the loop modeling, even if the volumetric heating rate is kept constant, and we will explore the diagnostics for different values of L .

The range of values of β considered here is from -2 to 2 . These values include the possibility of constant heating along the loop ($\beta = 0$), the predictions from the DC heating models ($\beta = 2$), and intermediate values that include predictions of the heating rate dependence on B from the AC models. Since B decreases with height, a positive β gives heating concentrated near the footpoints. We have therefore also included negative

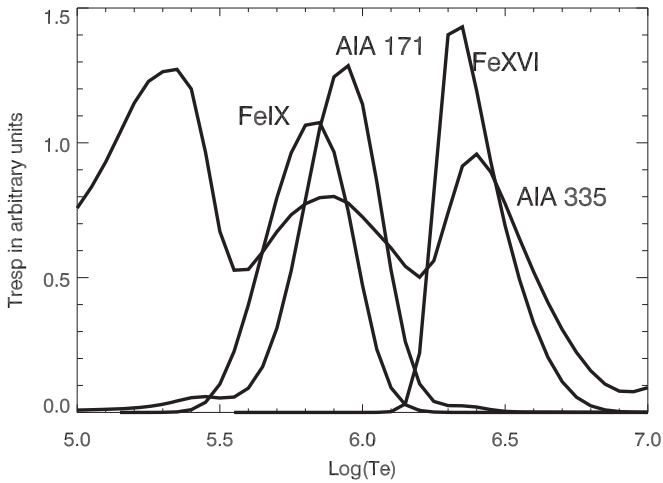


Figure 3. Temperature response of the considered *SDO/AIA* filters, 171 and 335, and spectral lines Fe IX 171 Å and Fe XVI 335 Å.

values of β , which give heating concentrated near the loop top, as often considered in the past. We vary β with a step of 0.1, and for each β we adjust Q_a to obtain a desired loop-top temperature T_{\max} . We consider values of T_{\max} in the range 1.0–2.5 MK to study the 1.0 MK loops seen in the Fe IX 171 Å and the 2.0 MK loops seen in the Fe XVI 335 Å band.

As stated in Section 1, in this study we are concerned with developing a diagnostic technique for a single loop that could be used to obtain the value of the power index β that best models the observed emission.

2.3. Modeling the Coronal EUV Emission

In order to facilitate a future comparison of the modeled active-region loops with real loops observed by current or past instruments, the EUV emission is modeled in two different channels, the 171 Å and 335 Å used by *SDO/AIA*, and the pure spectral lines Fe IX 171 Å and Fe XVI 335 Å. The Fe XVI lines were routinely observed by the *SOHO* Coronal Diagnostic Spectrometer at 360.8 Å (Fludra & Ireland 2003, 2008) and also at 335 Å, while the Hinode EIS spectrometer (Culhane et al. 2007) observes Fe XVI 263.0 Å and Fe IX 171 Å.

The temperature response for the AIA channels has been calculated by Lemen et al. (2012) and is available in the solarsoft library. The emissivity of the Fe IX 171 and Fe XVI 335 Å spectral lines has been derived using the ADAS package (Summers 2001) and is also available in Chianti (Dere et al. 2009). The response functions for the AIA 171 and 335 channels and the Fe IX 171 Å and Fe XVI 335 Å lines are shown in Figure 3. The electron temperature and density of the plasma were then modeled along each of the loops in the active region for different values of Q_a and β as described in the previous section, and these parameters were convolved with the response functions of the various lines to give the modeled emission. When modeling single loops, we explore a large parameter space of Q_a and β , for each β selecting a value of Q_a to obtain a desired peak temperature, for example, 1 MK or 2 MK.

It is also possible to simulate emission from all loops in the region to get an overall impression of how the modeling works. When simulating the entire active region, we use the full Equation (4) with the actual loop length L , adopting $\lambda = -1$ as suggested by Fludra & Warren (2010). We then use the same Q_a and β for all loops, which gives a distribution of peak

temperatures, and we select a value of Q_a to move the peak of the temperature distribution to approximately cover the range of observed temperatures between 1 MK and 2 MK. The EUV emission from these loops in the selected four wavelengths is then modeled by convolving the N_e and T_e distributions with the temperature responses of *SDO/AIA* and the pure spectral lines. Here, we do not fit Q_a and β to exactly match the entire active-region emission in one or more bands, as done for example by Dudik et al. (2011). Instead, we use a plausible pair of Q_a and β to illustrate the principle of our modeling.

Once this modeled emission had been calculated for all loops, it is then projected on a 2D plane in the same manner as would be observed by *SDO/AIA*, as shown in Figure 1(a). If we intended to perform a rigorous one-to-one comparison of the model to the observations, the simulated image would be additionally smeared with the spatial point-spread function. Here, we dispense with this step since this simulation is not being compared to data. Line-of-sight effects are accounted for by assuming that our loops at the top are narrower than the pixels and therefore assigning the total intensity of each loop section to the nearest pixel. While this assumes that the loop expansion takes place inside a pixel, it provides a better resolution of the fine structure of the modeled magnetic field and is qualitatively in agreement with the reported constant cross sections of loops observed in the 171 Å emission. This can be compared to the observed AIA 171 Å image in Figure 2(a). It is important to note that there are several differences between the modeled and observed images, due to the limitations of the model. First, the longer loops on the right-hand side and in the bottom left-hand corner are not modeled in the artificial image because they leave the volume of the modeled data cube, hence the black areas of this image in Figure 1(a). These long loops are either open magnetic field lines or they close outside the modeled volume. Very short loops, not reaching 2 Mm height, are also not included. There is also background emission possibly from the coronal moss that is not modeled in the artificial image, as this is coming from the legs of the hot loops that are not present in the assumed model due to centering the peak temperature distribution around 1.0 MK.

3. RESULTS

3.1. Diagnostics of the Heating Function

As stated in Section 1, the aim of this paper is to develop a diagnostic technique to identify the power index, β , in Equation (4) by comparing models of individual loops to coronal images. We are seeking to develop a measurable quantity that could provide a quantifiable comparison. We are comparing loops with the same maximum temperature as the narrow-band EUV filters, or spectral lines will only show loops that have similar temperatures.

There are two potential ways to diagnose the coronal heating: either through measuring plasma parameters inside coronal loops (electron temperature and density) or measuring the observed emission in the narrow EUV bands or intensities of spectral lines.

Diagnostics based on an observation in a single spectral line have obvious limitations, the first of which is a lack of precise information about the loop-top temperature. Figure 4 shows the emission in the Fe XVI 335 Å line along loop B for a fixed value of $\beta = 0.5$ but varying Q_a . The values of Q_a were

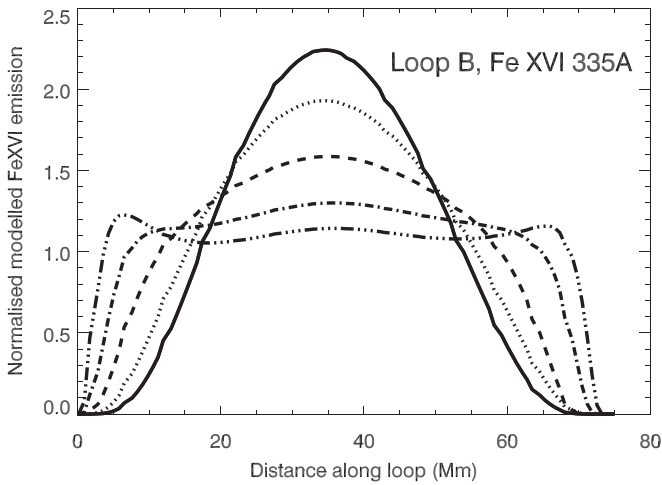


Figure 4. The variation of normalized modeled emission in the spectral line Fe XVI 335 Å along loop B for $\beta = 0.5$. The solid line has a peak temperature of 1.5 MK, the dotted line 1.75 MK, the dashed line 2.0 MK, the dot-dashed line 2.25 MK, and the triple-dot-dashed 2.5 MK.

selected so as to fix the peak temperature in the loop at $T_e = 1.5, 1.75, 2.0, 2.25, 2.5$ MK. The peak of emission is initially located at the top of the loop, with very limited emission toward the footpoints. As the peak temperature increases, the proportion of the loop significantly emitting increases. As the peak temperature rises further, the emission at the center of the loop drops off, and two peaks of emission form and move toward the footpoints of the loop. This overall behavior is as described in Fludra & Ireland (2003), and it provides a qualitative indication of the increasing temperature. This behavior is also seen to a lesser extent in the 335 Å AIA filter; it is not as pronounced because the emission peak for this filter is much broader than the pure Fe XVI (which is the primary ion in the 335 Å filter). The distribution of intensity along the loop, varying from strongly peaked near the loop top to flat or even double-peaked near the footpoints, can, therefore, provide an indication of the temperature in the range 1.5–2.5 MK, provided other parameters do not affect the intensity distribution. Below we address more sophisticated diagnostic possibilities, assuming in simulations that the loop-top temperature is 2.0 MK for the Fe XVI line and 1.0 MK for the Fe IX line.

Temperature distributions along the loop for different values of β and $T_{\text{top}} = 2$ MK in loop B are shown in Figure 5(b). While the distributions for different values of β are quite similar, some change can be seen near the footpoints: as β increases, the loop becomes more isothermal. For example, comparing values at a distance $s = 0.25L_{1/2}$ from the left footpoint, the temperature changes from 1.4 MK to 1.7 MK when β changes from -2 to 0.5 . For such a change to be detectable by observation, the 1σ error of the temperature determination would need to be less than 0.1 MK. For a loop with $T_{\text{top}} = 1.0$ MK (Figure 6(b)), at the same distance from the footpoint the temperature changes from 0.8 MK to 0.92 MK when β increases from -2 to 1.0 . In this case, the 1σ temperature measurement error would need to be as small as 0.04 MK to reliably detect such a change. Typical temperature measurement errors achievable with present instruments are illustrated in Aschwanden et al. (2008), who determined temperatures of 30 loops from STEREO observations in the 171 and 195 Å bands, concluding that they are isothermal

along the loops, with a standard deviation of between ± 0.17 MK and ± 0.39 MK for temperatures between 0.9 MK and 1.38 MK, respectively. These errors are greater than the temperature change in our simulation, making it difficult to determine such a small temperature change from observations.

Electron density distributions for the same two cases for loop B are shown in Figures 5(a) and 6(a). It is clear that the density change in the central part of the loop is much greater than the change in temperature. The loop-top density in Figure 5(a) changes from 1.8×10^9 to $4.1 \times 10^9 \text{ cm}^{-3}$ when β increases from -2 to 0.75 , and in Figure 6(a) from 0.4×10^9 to $1.0 \times 10^9 \text{ cm}^{-3}$ when β increases from -2 to 1.0 . In both cases, the increase is approximately by a factor of 2.3 and 2.5, respectively. Change of this magnitude can be measured easily provided that a suitable density diagnostic line ratio exists in the relevant temperature range and an EUV spectrometer including these spectral lines is part of the mission payload. Figure 7 shows the variation of N_e as a function of β for loops A, B, and C. This provides the primary diagnostics for β when the density can be measured from a density-sensitive line ratio.

The next measure to be considered was the total intensity of each loop. Since the intensity is proportional to N_e^2 , based on the previously discussed behavior of the density, we can expect a significant change of the intensity with β . The intensity for all points along the loop was summed, giving the total intensity in the loop in all selected lines. These are shown for all four loops in Figure 8. It was found that the behavior for loops A, B, and C was similar, whereas loop D shows somewhat different behavior, so we will initially limit discussion to loops A, B, and C. As β increases from 0 to 1 for loops A, B, and C, the total intensity for all lines rises steeply by over a factor of roughly 3, being clearly sensitive to the increasing concentration of heating toward the footpoints. In contrast, for values of β decreasing from 0 to -2 , there is only a 40% decrease in the total intensity. As the heating distribution changes from a uniform heating to one concentrated near the loop top, the conductivity efficiently redistributes the heat along the loop. While the 40% change between $\beta = -2$ and $\beta = 0$ is measurable, the error bars on the derived β in this range would be significantly greater than in the range $0 < \beta < 1$. We note that the curves in Figure 8 are normalized to 1 for $\beta = 0$, and we assume the loop filling factor $f = 1.0$. If the filling factor was known, this would be an obvious diagnostic suitable for imaging instruments that measure intensities in narrow EUV bands, without the support of spectroscopic observations, and also for spectral line intensities when the density diagnostic is not available. However, in practice, the filling factors are usually not known and have to be derived as an additional free parameter when comparing the modeled images with observations. Therefore, the unnormalized versions of the curves from Figure 8 would need to be multiplied by the actual value of f to be used for the diagnostics.

We have also tested the sensitivity of the shape of the intensity distribution along the loops to β . Figures 6(d) and 5(d) show the normalized intensity along the loop for different values of β for both the AIA bands 171 and 335. While there are some differences between these distributions, they appear to be too small to distinguish between different values of β , especially in the expected presence of measurement errors in real data. The same normalized intensity distributions for the

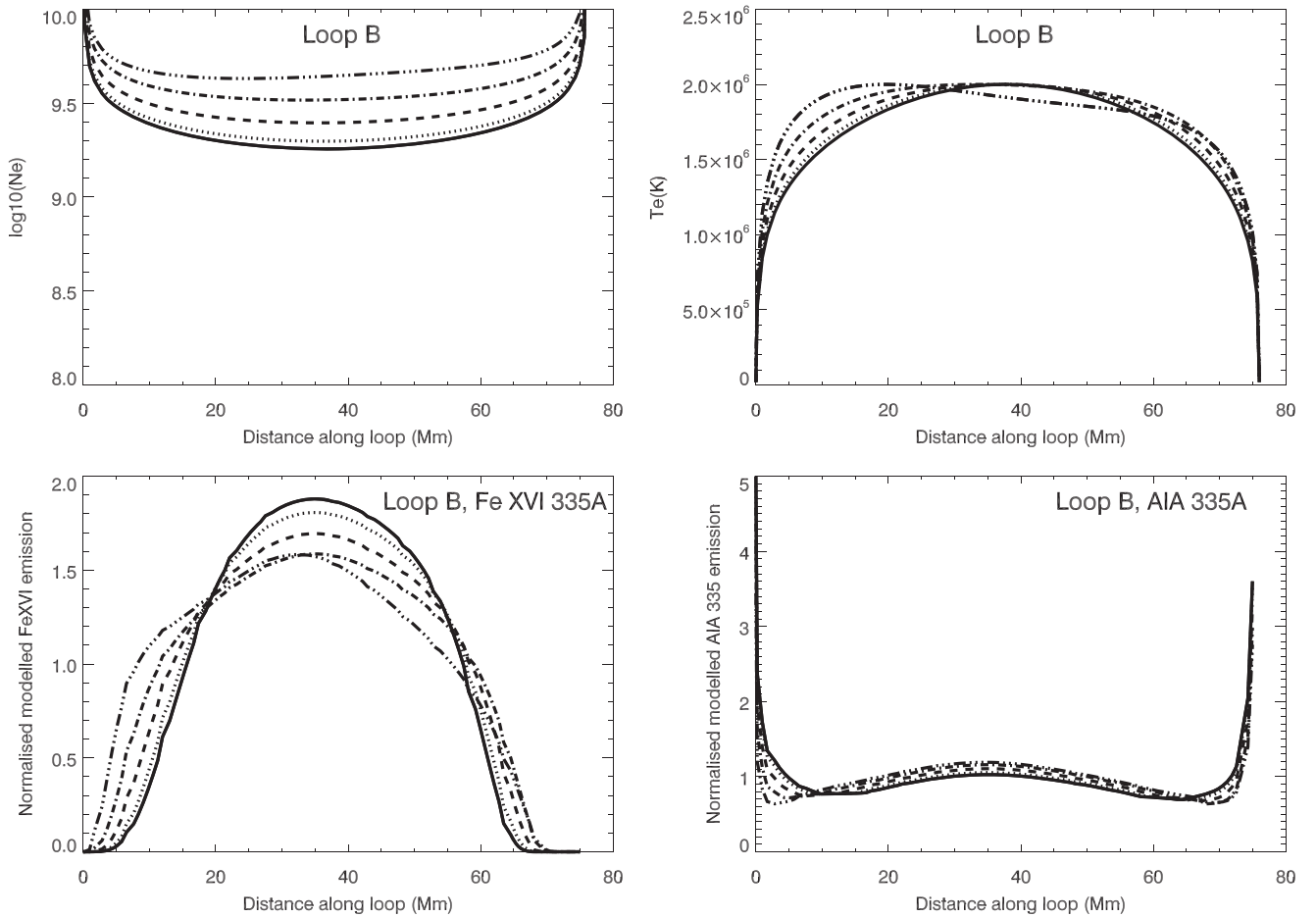


Figure 5. Results of modeling loop B for different values of β and with the peak temperature fixed at 2 MK. In all plots, the solid line represents $\beta = -2.0$, the dotted line $\beta = -1.0$, the dashed line $\beta = 0.0$, the dot-dashed line $\beta = 0.5$, the triple-dot-dashed line $\beta = 0.75$. The top left panel shows the electron density along the loops for these different parameters. The top right panel shows the electron temperature, bottom left shows the Fe XVI 335 Å emission, and bottom right shows the SDO/AIA 335 Å band emission.

pure Fe IX 171 and Fe XVI 335 Å line emission are shown in Figures 6(c) and 5(c). We conclude that the normalized spatial distributions along the loops are too similar to provide the required diagnostics. While the emission from the pure ions is slightly more sensitive to variations in β , overall the shape of the normalized intensity curves is still not sensitive enough to be a useful diagnostic.

The above discussion points to the following diagnostic suitable for single loops: the electron density measured directly from density-sensitive line ratios. We have found that, in our heating model given by Equation (4), the dependence of the electron density on β is related to how the magnetic field strength varies along the loop. The magnetic field strength of most of the loops we have considered cannot be approximated by a single component decaying exponentially from the footpoint toward the apex. Instead, the local magnetic scale height tends to increase with distance from the footpoint, and the field has a nonzero value at the loop top. Nevertheless, for loops A, B, and C, their magnetic field decreases steeply with height, reaching a low level of the loop-top component. For this type of $B(s)$, the resulting $I_{\text{tot}} - \beta$ dependence shows a loss of stable solutions occurring close to $\beta = 1$ (see Section 3.2 for further discussion). The magnetic field along loop D, however, decays less steeply and has a significantly higher level at the loop top, which increases the range of β for which stable solutions exist. In the extreme case, if the magnetic field

strength is nearly constant along the loop, the heating rate $E_H \propto B(s)^\beta$ would vary very little along the loop even for large values of β , resembling the case of a nearly constant heating rate. Such loops are found to have stable solutions up to large values of $\beta > 10$ but offer very little diagnostic capability in the range $0 < \beta < 2$. A survey of a number of loops in the active region under study reveals that such loops with a flat distribution of $B(s)$ indeed appear to exist, particularly for shorter lengths below 60 Mm. Therefore, the diagnostic presented in Figure 7 is applicable only to loops with steeply decreasing $B(s)$.

3.2. Loss of Stable Solutions

In Figures 7 and 8 we restricted the range of β to below 1.0. The reason is that for larger values of β the hydrostatic code does not find a stable solution for loops A, B, and C. Serio et al. (1981), Aschwanden et al. (2001), Winebarger et al. (2003), and Schrijver & van Ballegoijen (2005) pointed out that for certain heating rates there is no steady solution of the energy-balance equation. We investigate how the loss of stability depends on the maximum loop temperature. Figure 9 shows the largest maximum temperature for each value of β for which a stable solution exists for loops A and B. The plot shows the temperature range $5.0 < \log_{10}(T_e) < 7.0$ as this fully covers the temperature range of interest. Both loops show

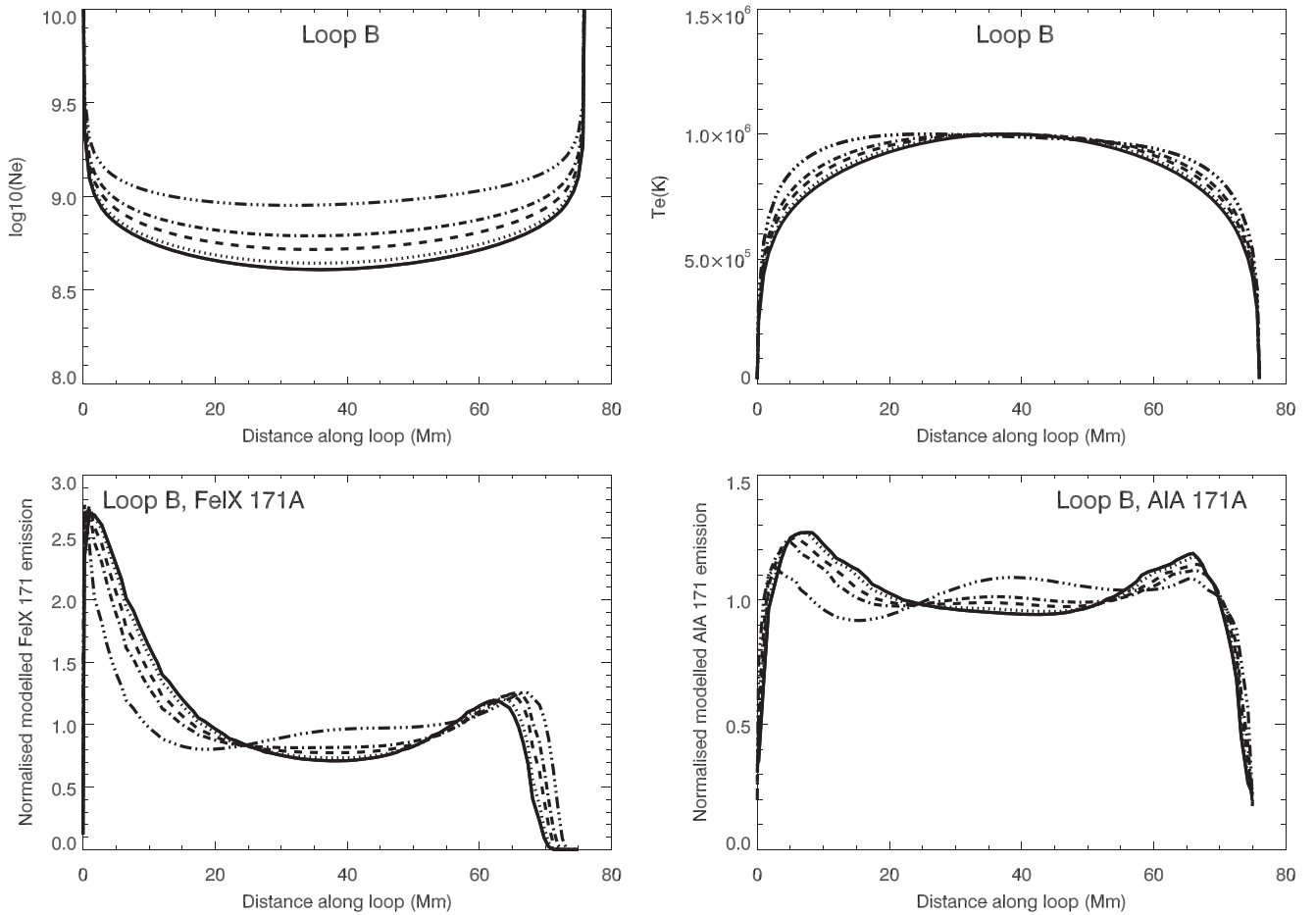


Figure 6. Results of modeling loop B for different values of β and peak temperature fixed at 1 MK. In all plots, the solid line represents $\beta = -2.0$, the dotted line $\beta = -1.0$, the dashed line $\beta = 0.0$, the dot-dashed line $\beta = 0.5$, and the triple-dot-dashed line $\beta = 1.0$. The top left plot shows the electron density along the loops for these different parameters. The top right plot shows the electron temperature, the bottom left plot shows the Fe IX 171 Å emission, and the bottom right plot shows the SDO/AIA 171 Å band emission.

similar behavior, with the maximum allowable temperature rapidly dropping from above $\log_{10}(T_e) = 7.0$ to just ~ 6.3 , that is, ~ 2 MK, in the range 0.6–0.7 for loop B and 0.8–0.9 for loop A. The curves then flatten out and fall below 1 MK for $\beta = 1.1$ and 1.2, respectively.

This thermal instability occurs as the heating becomes more concentrated toward the footpoints, and the peak temperature is no longer located at the top of the loop, which leads to coronal condensation and a rapid cooling of the plasma at the peak of the loop. The loop then undergoes a condensation–evaporation cycle with significant plasma flows (e.g., Mok et al. 2008). This instability was studied analytically by Serio et al. (1981) for a half-loop with an exponentially decreasing heating function. They found that the loops became unstable when the scale height of the heating rate, s_H , was approximately one-third the loop half-length. We postulate that this is the same instability that is causing our loops to become unstable at higher temperatures and values of β . Other estimates of the critical heating scale height were derived by Aschwanden et al. (2001) and Winebarger et al. (2003). Unfortunately, a direct comparison to these criteria is not possible as a pure exponential function is not a good fit to $B(s)$, and hence also to our heating rate, and, in addition, loops are not symmetric. We have found that the magnetic field strength drops by a factor of $1/e$ with a scale height of ~ 2.8 Mm in one of the footpoints of loop B and 5.5 Mm in the other footpoint. For

other loops we found values of around ~ 5 to ~ 16 Mm. Some of these values are much smaller than the $L/3$ suggested by Serio et al. (1981); however, the nonzero component of $B(s)$ at the loop top ensures that there is always a significant fraction of heating occurring at the loop apex, so the fast-decreasing field near the footpoint must be significantly steeper to trigger the instability.

This study of the existence of static solutions for a given heating rate can also provide information on the nature of the heating mechanism. Table 5 in Mandrini et al. (2000) provides a list of possible heating mechanisms and their expected heating rate. This list suggests that DC heating mechanisms tend to have a value of $\beta = 2$, which for the loops we are considering would not provide a static solution. For example, as demonstrated by Lionello et al. (2013), the heating function $E_H(s) \propto B(s)^{7/4}$ leads to thermal instability. However, the heating rates for AC heating mechanisms usually have values of $\beta \leq 1$, suggesting that these mechanisms could provide stable solutions for the loops considered here.

3.3. Discussion

We have shown that the electron density is a useful diagnostic parameter sensitive to the location of the heating. It can provide a diagnostic of the heating rate free of the assumptions of the loop filling factor. We have expanded on

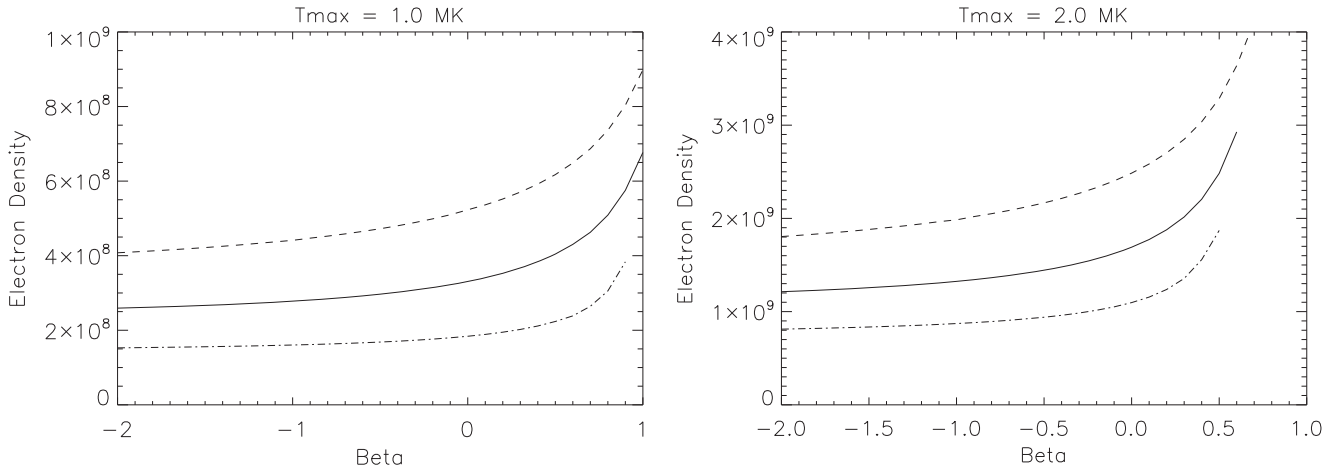


Figure 7. The variation of electron density with β for the loop-top temperature of 1.0 MK (left panel) and 2.0 MK (right panel). The solid line is loop A, the dashed line is loop B, and the dot-dashed line is loop C. Density units are cm^{-3} .

the previous results available in the literature, assuming a heating rate with a power-law dependence on the local magnetic field strength along the loop, and we have shown that the power-law index β can be determined for $\beta \leq 1$. For greater values of β , thermal instability leads to unstable solutions. We present, for the first time, a quantitative illustration of the effect of the thermal instability on the relationship between the maximum loop-top temperature and the index β (Figure 9).

While in the last two decades three instruments had the capability to measure coronal electron densities in active regions (*SOHO* Coronal Diagnostic Spectrometer, *SOHO*/SUMER, and Hinode/EIS), observations of well-resolved loops in density-sensitive lines are rare.

Ugarte-Urra et al. (2005) measured N_e from density-sensitive Fe XIV lines along a loop observed on the limb by *SOHO*/CDS. They find the density at the apex equal to $0.9 \times 10^9 \text{ cm}^{-3}$ for a loop with half-length $L = 7.2 \times 10^9 \text{ cm}$. The density stays nearly constant in the lower half of the loop, increasing by 40% at the footpoints. They ran a hydrodynamic model with a constant cross section and a parametric heating rate, $H_0 \exp(\lambda s)$, and calculated the equilibrium solutions. Varying the parameter λ and comparing the modeled density to their measurements, they find that the heating rate exponentially decreasing from the footpoints gives the lowest χ^2 . This supports the footpoint heating models discussed in our paper, although the magnetic field along the loop is not available. Importantly, Ugarte-Urra et al. (2005) demonstrate that a stable solution fits this loop.

However, this data set had only nine data points and relatively large error bars, particularly at the loop ends. It was reanalyzed by Adamakis et al. (2010), who, using a different statistical technique, reached an opposite conclusion that the heating distribution is apex-dominated. Adamakis et al. (2010) also analyze the X-ray observations of Priest et al. (2000) of a temperature distribution along a loop and also obtain an opposite conclusion to Priest et al. (2000), this time of footpoint-dominated heating. This application of different techniques illustrates the importance of improving the statistical accuracy of the measurements.

Another loop well observed by the Hinode/EIS spectrometer is discussed by Gupta et al. (2015), who analyze spectral lines sampling the upper transition region temperatures, with a loop-

top temperature of $7.3 \times 10^5 \text{ K}$. These authors compare the electron density distribution determined from Mg VII lines to that expected from a hydrostatic model, using a density scale height related to peak temperature. The modeled densities do not fully agree with the observed density change with height, being overdense in one leg and underdense in the other leg, possibly indicating that this loop is not in a static equilibrium.

In most observations of coronal loops taken with missions such as TRACE, STEREO, or *SDO*, the spectroscopic electron density diagnostics is unavailable, and the alternative way to diagnose the coronal heating is to use the spectral line or EUV band intensity. As the intensity is proportional to N_e^2 , it is even more sensitive to the change of the power-law index β , as shown in Figure 8. The main drawback, however, is that the loop filling factor needs to be known to apply this method. The large uncertainties of determining the filling factor are well documented in the literature (e.g., Reale 2014). For example, Ugarte-Urra et al. (2005) obtained the filling factor estimates of 0.1–0.7, dependent on the location along the loop and the spectral lines chosen to derive the emission measure. Dudik et al. (2011) obtained values from 0.06 to 0.25 in different spectral bands. Moreover, the authors typically assume that the filling factor is the same for all loops, which may not in fact be true. For the above reasons, the conclusions from past studies comparing the observed intensity distributions with simulated intensities and making assumptions about the loop filling factor need to be treated with caution.

The second conclusion from our study is a further quantifying of previous results available in the literature that the thermal instability is triggered when the heating rate is increasingly concentrated near the footpoints. We find that for realistic loop models with an asymmetric distribution of the magnetic field and nonpotential fields, the actual criterion for triggering the thermal instability will vary from loop to loop. Approximately, however, in the heating model used in this paper, this happens when the power index β is in the range 0.6–1.0. This leads to the following important conclusion: if a loop is found in a stationary state and with a peak temperature greater than 1 MK, it is likely to be heated by one of the AC mechanisms (Mandrini et al. 2000).

The 3D MHD models of active regions mentioned in Section 1 use a DC Joule heating where the heating rate is proportional to the current density squared, which in turn is

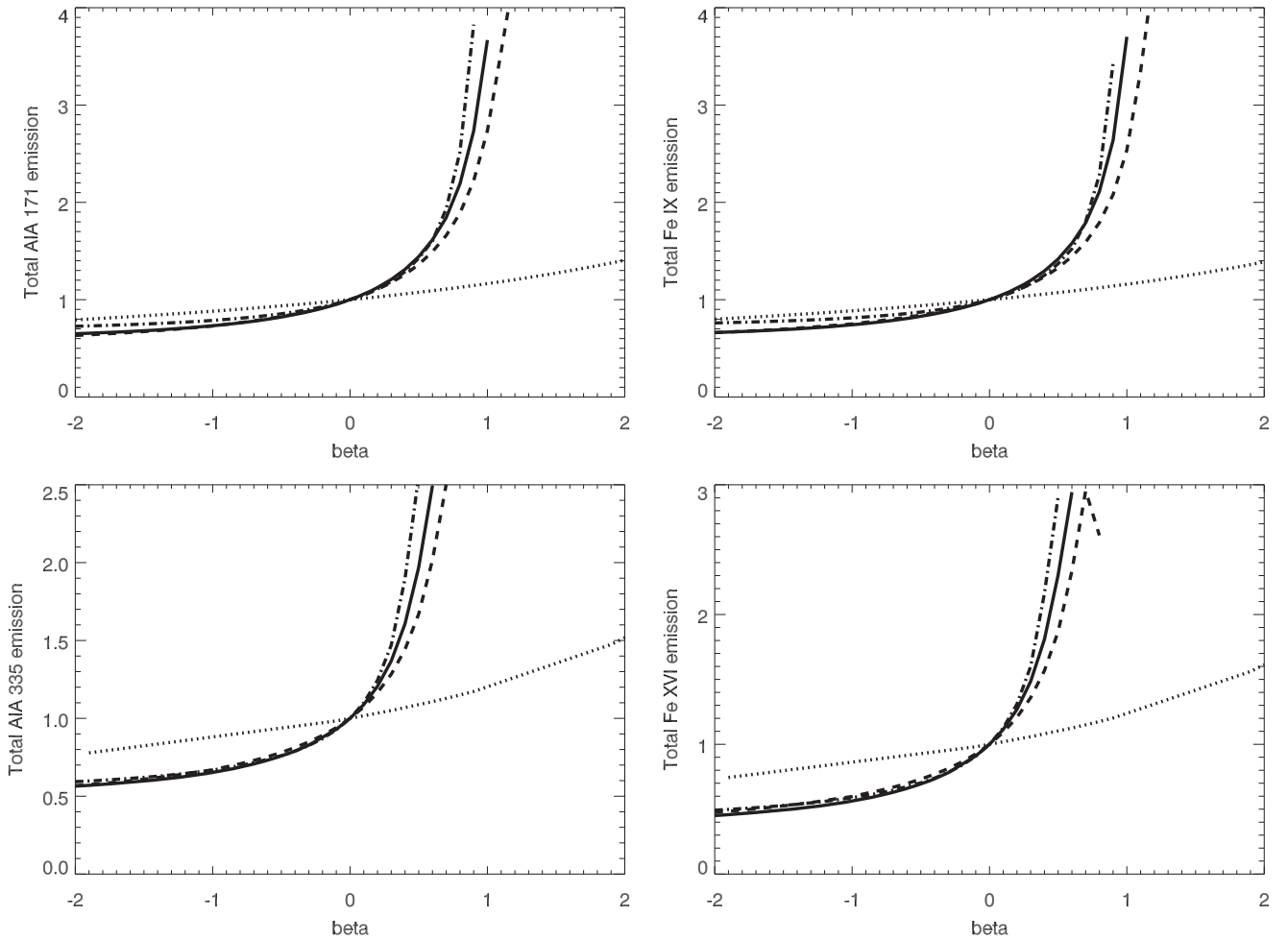


Figure 8. The variation of total modeled emission with β for all considered EUV filters. The top left plot is for the AIA 171 Å band. Top right shows pure Fe IX 171 Å. Bottom left is the AIA 335 Å band. Bottom right is pure Fe XVI 335 Å. The solid line is loop A, the dashed line is loop B, the dot-dashed line is loop C, and the dotted line is loop D. All of the curves are normalized to 1 for $\beta = 0$. The loop filling factor is assumed equal to 1.0.

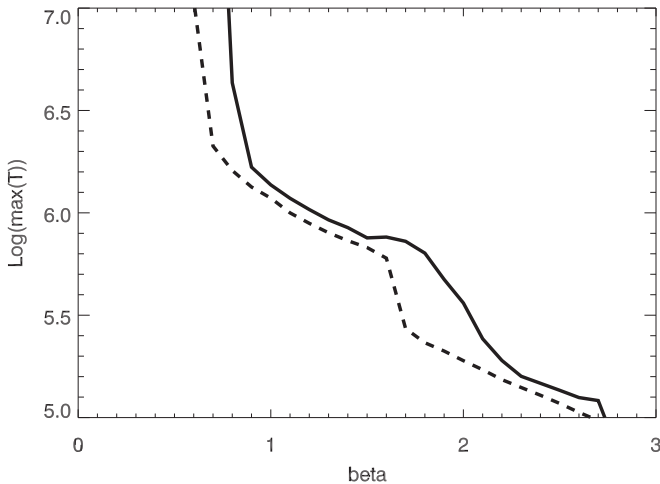


Figure 9. The variation in maximum temperature with β for stable solutions found for loop A (continuous line) and loop B (dashed line).

proportional to the local magnetic field strength squared, $B^2(s)$, and decreases exponentially with height (Gudiksen & Nordlund 2005). These models predict a dynamic state of the modeled loops that agrees with our result since these models are equivalent to our case $\beta = 2$. Therefore, if the footpoint braiding is the only or dominant mechanism of heating the

active-region loops, these loops will be thermally unstable and fall outside the range of the diagnostics considered in this paper.

It is, however, possible that the corona contains both stable and unstable loops. Fludra & Warren (2010) have found from the analysis of the transition-region emission at temperatures around 2×10^5 K that about 25% of loops at these temperatures are stationary, consistent with the heating mechanism with $\beta = 0.5$. The remaining 75% of loops show the presence of additional, time-variable heating. This analysis is quite rare among the past studies as it uses the transition region spectral line of O V 62.9 nm, where the spatial distribution of its intensity can be compared more accurately to the underlying magnetic field. Moreover, this observational estimate of the heating rate of the stationary heating finds a theoretical support in a heating mechanism described by van Ballegooijen et al. (2011), where the energy dissipation occurs through Alfvén wave turbulence. Their Equation (61) predicts an “equilibrium” heating rate proportional to $B_{cor}^{0.55} \text{ erg cm}^{-3} \text{ s}^{-1}$. This model far exceeds in sophistication the early estimates of various heating models presented by Mandrini et al. (2000) and is therefore a serious candidate for the heating mechanism.

The review of past observational studies of coronal heating highlights a number of difficulties. On the one hand,

observations suggest that the power index β ranges from 0.5 to 1.0. However, some of the studies (e.g., Schrijver et al. 2004) suggesting $\beta = 1$ used simplified assumptions of uniform heating and potential magnetic fields, while Warren & Winebarger (2006) showed that a uniform heating that best matches soft X-ray observations cannot simultaneously reproduce the observed EUV emission of the active region. A further problem with the uniform heating is a possible contradiction: while it makes the heating rate independent of the local magnetic field $B(s)$ along the loop, it still assumes that the heating rate depends on the magnetic field B_{phot} at the footpoints.

Statistical studies using fully resolved images of active regions or the full disk report a lack of a unique goodness-of-fit criterion: different results are obtained when matching the temperatures and emission measures from X-ray filter ratios, and different results come from looking at the subjective quality of visually reproducing the structure of the active region (e.g., Lundquist et al. 2008a,b). There is also a generally acknowledged difficulty in simultaneously reproducing X-ray and EUV emission (e.g., Dudik et al. 2011), with a suggestion that possibly a majority of EUV loops are in a dynamic state. On the other hand, 3D MHD models assume a Joule heating mechanism ($\beta = 2.0$) and present a picture of a dynamically evolving corona that looks qualitatively visually convincing but so far do not find support in observational estimates of the power index β .

The future strategy to remove the current confusion and achieve further progress should involve a combination of several approaches, listed here in order from simple to the most complex. (1) Search for well-isolated stationary loops, observed using density-sensitive spectral lines, to provide a diagnostic - based on Figure 7. Such loops may have possibly been observed by the Hinode/EIS spectrometer, while the proposers of future missions would need to ensure that EUV spectrometers with a suitable spectral range are part of the payload. (2) Use multiple stationary loops simultaneously, with different values of B_{phot} at their footpoints and different loop lengths. This would also allow a derivation of the parameter λ in Equation (4). (3) Models of dynamic loops should be incorporated into the diagnostics, as was suggested by Dudik et al. (2011), without, however, providing sufficient detail in their paper to enable reproducing their results. (4) Finally, in parallel to the points above, a growing sophistication of the 3D MHD models may eventually lead to these models accurately reproducing the magnetic structure and the emission of the active regions and enabling a quantitative comparison to observations. For any of the above approaches to work, the vector magnetic field measurements need to be available to provide a reliable extrapolation of the magnetic field along the loops.

Given the rarity of the measurements of the density-sensitive spectral lines needed for the above approaches and the abundant availability of observations in normal EUV lines, narrow-band EUV images, or X-ray images, some researchers will no doubt repeat the past studies described in Section 1. Unfortunately, the unknown loop filling factors will continue to pose a challenge, and such analyses have already been shown to lead to contradictory results. One can only suggest that a more discerning analysis should be made to avoid a wholesale fitting of the full Sun images or even the entire active regions, but instead find ways to separate stationary loops from dynamic loops.

4. CONCLUSIONS

We have reviewed and critically analyzed past results from the literature on the determination of the coronal heating mechanism. In our view, the attempts of the past few decades to find the coronal heating mechanism using X-ray and EUV observations have ended in a mild crisis. Past analyses report problems with matching the modeled emission to observations and suffer from unknown filling factors, a general inability of the magnetic field extrapolations to precisely match the observed coronal loops (noticeable both in potential field extrapolations but also in NLFF extrapolations), the inclusion of loops undergoing thermal instability, and possibly too simple a formula for the heating function used in the modeling that does not allow for the presence of more than one heating mechanism. New, more refined approaches are needed to provide observational constraints on the coronal heating models. We present one of them, applicable to single, well-isolated loops.

We have carried out simulations of coronal loops of moderate lengths in a solar active region, seeking a diagnostic method for the dependence of the coronal heating rate on the magnetic field strength along the loop. Our aim has been to ascertain whether observations of selected individual coronal loops made in the EUV wavelengths are capable of providing constraints on the coronal heating model. To reduce the number of free parameters and arbitrary assumptions, we have considered a quasi-static model applicable to approximately 30% of EUV loops observed in active regions. Considerations of time-variable heating or dynamic loop models for overdense loops (Aschwanden et al. 2001) have been deferred to a future paper.

Starting with a photospheric vector magnetogram from *SDO*/HMI, the coronal magnetic field was modeled using an NLFF extrapolation code. The geometry of this field was compared to an *SDO*/AIA 171 image of the same active region, and four loops that matched well were identified. The plasma in these loops was then modeled using a 1D stationary model capable of applying an arbitrary heating rate as a function of magnetic field strength along the loop. The heating rate was varied as a function of the power index β (Equation (4)), and the plasma parameters and the EUV emission in four wavelengths, the *SDO*/AIA 171 and 335 bands and the pure Fe IX 171 Å and Fe XVI 335 Å spectral lines, were derived along the loop for each β .

We have arrived at the following conclusions about the possible diagnostics of the heating rate in a single loop, similar in loops with peak temperatures of 1 MK and 2 MK:

1. In the subset of steady-state loops considered in this paper, for a fixed loop-top temperature of $T_{\text{top}} = 1.0$ MK, the temperature difference near loop footpoints is only 0.12 MK for β between -2 and 1.0. For $T_{\text{top}} = 2.0$ MK, the electron temperature near footpoints varies by 0.3 MK for a range of β between -2 and 0.75. Such differences are smaller than the error of temperature determination from the EUV filter ratios of current instruments, so they cannot reliably distinguish between different values of β .

2. A significantly more sensitive plasma parameter is the electron density, which changes by a factor of up to 2.6 when β changes from -2 to 1. If the density can be determined from spectroscopic measurements using density-sensitive line ratios, it can provide a diagnostic of β for $\beta \leq 1$, provided the loop length is known. This is the only diagnostic for a single loop

that does not require the knowledge of the filling factor. Therefore it can be applied to individual loops and allows the determination of both the power index β and the filling factor.

3. The total intensity of the EUV emission summed along the loop is therefore also sensitive to β . However, since the filling factor is usually not known, the intensity measurements in a single loop cannot provide the diagnostics of the heating rate, and all past studies comparing observed intensity distributions with simulated intensities suffer from this problem.

4. The range of sensitivity for β , of both the electron density and the line intensity, depends on the shape of the distribution of the magnetic field strength along the loop. For $B(s)$ steeply decreasing from the footpoint and reaching low values near the loop top, the best diagnostic range is $0 < \beta < 1$, where the density increases by up to a factor of 2, providing a clear distinction between a uniform heating and the heating concentrated near the footpoints, and allowing the measurement of the value of β . For the heating concentrated near the loop top ($-2 < \beta < 0$), the change of the density is up to 30%. This is measurable, but due to the flat nature of this part of the curve, the error bars on the determined values of β would be much larger.

5. For this category of loops with a steeply decreasing $B(s)$, when the heating becomes strongly concentrated near the footpoints ($\beta > 1$), there are no more stable solutions.

6. For loops with a flat distribution of $B(s)$ over a significant portion of the loop, the range of β for which stable solutions exist increases and can reach values from 4 to 16 as $B(s)$ becomes progressively more constant. However, values of β greater than 2 are less interesting for the diagnostic of coronal heating, and the normalized intensities for these loops change little for $\beta < 2$.

7. For loops considered in item 3 above, if their heating rate depends locally on the magnetic field as in Equation (4), the heating mechanisms that give stable static solutions ($\beta < 1$) are likely to be AC heating models (Mandrini et al. 2000). The DC heating models with $\beta = 2$ would lead to dynamic solutions.

8. Finally, we point out a striking agreement between a rare observational study of Fludra & Warren (2010) and a detailed theoretical model of heating through Alfvén wave turbulence (van Ballegooijen et al. 2011), which both give the index $\beta \approx 0.5$. According to Fludra & Warren (2010), this quasi-stationary basal heating can be detected in about 25% of loops seen at transition-region temperatures, while the remaining loops show the presence of additional time-variable heating.

Based on the analysis carried out in this paper, it is highly recommended that future solar missions carry EUV spectrometers capable of providing density diagnostics at coronal temperatures.

CH was supported by a studentship from the University of Warwick and the Science and Technology Facilities Council (STFC). AF's work was supported by the STFC. The authors thank Dr. T Wiegmann for providing the NLFF extrapolation software, Dr. A van Ballegooijen for the loop modeling software, and Dr. Xudong Sun for providing the HMI magnetograms. VMN acknowledges the support from the STFC Warwick Astrophysics Consolidated Grant ST/L000733/1 and the European Research Council under the SeismoSun Research Project No. 321141.

Facility: SDO.

REFERENCES

- Adamakis, S., Walsh, R. W., & Morton-Jones, A. J. 2010, *SoPh*, **262**, 117
- Amari, T., Aly, J. J., Luciani, J. F., Boulmezaoud, T. Z., & Mikic, Z. 1997, *SoPh*, **174**, 129
- Aschwanden, M. J. 2004, *Physics of the Solar Corona* (Berlin: Springer)
- Aschwanden, M. J. 2013, *SoPh*, **287**, 323
- Aschwanden, M. J., Nitta, N. V., Wuelser, J.-P., & Lemen, J. R. 2008, *ApJ*, **680**, 1477
- Aschwanden, M. J., Schrijver, C. J., & Alexander, D. 2001, *ApJ*, **550**, 1036
- Culhane, J. L., Harra, L. K., James, A. M., et al. 2007, *SoPh*, **243**, 19
- Dere, K. P., Landi, E., Young, P. R., et al. 2009, *A&A*, **498**, 915
- Dudik, J., Dzifcakova, E., Karlicky, M., & Kulinova, A. 2011, *A&A*, **531**, A115
- Fisher, G. H., Longcope, D. W., Metcalf, T. R., & Pevtsov, A. A. 1998, *ApJ*, **508**, 885
- Fludra, A., & Ireland, J. 2003, *A&A*, **398**, 297
- Fludra, A., & Ireland, J. 2008, *A&A*, **483**, 609
- Fludra, A., & Warren, H. 2010, *A&A*, **523**, A47
- Galsgaard, K., & Nordlund, A. 1996, *JGR*, **101**, 13445
- Gary, G. A. 2001, *SoPh*, **203**, 71
- Golub, L., Maxson, C., Rosner, R., Vaiana, G. S., & Serio, S. 1980, *ApJ*, **238**, 343
- Gudiksen, B. V., & Nordlund, A. 2005, *ApJ*, **618**, 1020
- Gupta, G. R., Tripathi, D., & Mason, H. E. 2015, *ApJ*, **800**, 140
- Gurman, J. B., Withbroe, G. L., & Harvey, J. W. 1974, *SoPh*, **34**, 105
- Hansteen, V., Guerreiro, N., De Pontieu, B., & Carlsson, M. 2015, *ApJ*, **811**, 106
- Klimchuk, J. A. 2006, *SoPh*, **234**, 41
- Lemen, J. R., Title, A. M., Akin, D. J., et al. 2012, *SoPh*, **275**, 17
- Lionello, R., Winebarger, A. R., Mok, Y., Linker, J. A., & Mikic, Z. 2013, *ApJ*, **773**, 134
- Lundquist, L. L., Fisher, G. H., & McTiernan, J. M. 2008a, *ApJS*, **179**, 509
- Lundquist, L. L., Fisher, G. H., Metcalf, T. R., Leka, K. D., & McTiernan, J. M. 2008b, *ApJ*, **689**, 1388
- Mandrini, C. H., Demoulin, P., & Klimchuk, J. A. 2000, *ApJ*, **530**, 999
- Metcalf, T. R., De Rosa, M. L., Schrijver, C. J., et al. 2008, *SoPh*, **247**, 269
- Mikic, Z., Lionello, R., Mok, Y., Linker, J. A., & Winebarger, A. R. 2013, *ApJ*, **773**, 94
- Mok, Y., Mikic, Z., Lionello, R., & Linker, J. A. 2008, *ApJL*, **679**, L161
- Narain, U., & Ulmschneider, P. 1996, *SSRv*, **75**, 453
- Parker, E. N. 1988, *ApJ*, **330**, 474
- Pevtsov, A. A., Fisher, G. H., Acton, L. W., et al. 2003, *ApJ*, **598**, 1387
- Priest, E. R., Foley, C. R., Heyvaerts, J., et al. 2000, *ApJ*, **539**, 1002
- Rappazzo, A. F., Velli, M., Einaudi, G., & Dahlburg, R. B. 2008, *ApJ*, **677**, 1348
- Reale, F. 2014, *LRSP*, **11**, 4
- Reale, F., Peres, G., Serio, S., et al. 2000, *ApJ*, **535**, 423
- Rosner, R., Tucker, W. H., & Vaiana, G. S. 1978, *ApJ*, **220**, 643
- Roumeliotis, G. 1996, *ApJ*, **473**, 1095
- Sakurai, T. 1981, *SoPh*, **69**, 343
- Scherrer, P. H., Schou, J., Bush, R. I., et al. 2012, *SoPh*, **275**, 207
- Schou, J., Scherrer, P. H., Bush, R. I., et al. 2012, *SoPh*, **275**, 229
- Schrijver, C. J., & Aschwanden, M. J. 2002, *ApJ*, **566**, 1147
- Schrijver, C. J., De Rosa, M. L., Metcalf, T. R., et al. 2006, *SoPh*, **235**, 161
- Schrijver, C. J., De Rosa, M. L., Metcalf, T. R., et al. 2008, *ApJ*, **675**, 1637
- Schrijver, C. J., Sandman, A. W., Aschwanden, M. J., & De Rosa, M. L. 2004, *ApJ*, **615**, 512
- Schrijver, C. J., & van Ballegooijen, A. A. 2005, *ApJ*, **630**, 552
- Serio, S., Peres, G., Vaiana, G. S., Golub, L., & Rosner, R. 1981, *ApJ*, **243**, 288
- Summers, H. P. 2001, *The ADAS manual*, version 2-3, <http://www.adas.ac.uk/>
- Ugarte-Urra, I., Doyle, J. G., Walsh, R. W., & Madjarska, M. S. 2005, *A&A*, **439**, 351
- van Ballegooijen, A. A., Asgari-Targhi, M., Cranmer, S. R., & DeLuca, E. E. 2011, *ApJ*, **736**, 3
- Vesecky, J. F., Antiochos, S. K., & Underwood, J. H. 1979, *ApJ*, **233**, 987
- Walsh, R. W., & Ireland, J. 2003, *A&ARv*, **12**, 1
- Warren, H. P., & Winebarger, A. R. 2006, *ApJ*, **645**, 711
- Warren, H. P., & Winebarger, A. R. 2007, *ApJ*, **666**, 1245
- Wheatland, M. S., Sturrock, P. A., & Roumeliotis, G. 2000, *ApJ*, **540**, 1150
- Wiegmann, T. 2004, *SoPh*, **219**, 87
- Wiegmann, T., Thalmann, J. K., Inhester, B., et al. 2012, *SoPh*, **281**, 37
- Winebarger, A. R., Warren, H. P., & Mariska, J. T. 2003, *ApJ*, **587**, 439